

# Microwave-Assisted Surfactant-Engineering Approach for Rapid Synthesis of Lithium–Manganese-Rich Oxide Cathode for Lithium Metal Batteries

Hansheng Li, M. Bilal Faheem, Madan Bahadur Saud, Bilawal Khan, Yuchen Zhang, Collin D. Rodmyre, Ruosi Qiao, Xinlu Wang, Phillip Hauck, Vanessa Kee, Poojan Kaswekar, Fan Zheng, Ian Dean Hosein, Jr-Hau He, Alevtina L. Smirnova, and Quinn Qiao\*

Lithium–manganese-rich oxides (LMRO) are competitive types of cathode materials for the next-generation lithium-ion batteries with high theoretical specific capacity and energy density. In this work, the LMRO cathode material is prepared through a rapid microwave assisted solvothermal process in combination with a commercially available surfactant, aimed to form crystal grains of uniform sizes within the reduced processing time. The microwave induces molecule vibrations throughout the reaction media, significantly boosts the intermolecular collisions, and

the surfactant micelles can regulate the sizes of crystalline seeds. The optimized quantity of surfactant enables the precipitation process to be further accelerated, and the final product with increased *R-3m* phase exhibited  $210 \text{ mAh g}^{-1}$  at  $100 \text{ mA g}^{-1}$  and a capacity retention of about 83.89% over 100 charge–discharge cycles working with lithium metal anodes. These results suggest that surfactant inclusion and microwave processing can significantly boost the synthesis process of layered cathode materials with enhanced performance.

## 1. Introduction

Lithium batteries were initially commercialized in the early 1990s and have been subsequently widely used in consumer electronics and electrified mobility solutions. To achieve a higher level of energy density, high-capacity cathode, anode and novel electrolyte materials are being focused. On the anode side, Li metal and silicon nanoparticles show their significant advantages in terms of energy density compared with the commercialized graphite.<sup>[1]</sup> On the cathode side, layered lithium transition metal oxides, first

discovered for the electrochemical energy storing potentials as early as 1970s,<sup>[2]</sup> have now become one key type of cathode materials, competing with olivine-structured materials such as lithium iron phosphate ( $\text{LiFePO}_4$ ). Compared with  $\text{LiFePO}_4$ , layered lithium metal oxides can achieve a higher level of energy density ( $700\text{--}900 \text{ Wh kg}^{-1}$  versus  $540 \text{ Wh kg}^{-1}$ ), preferable for extended recharge intervals for consumer electronics and electric vehicles. Starting from the  $\text{LiCoO}_2$ ,<sup>[2a,3]</sup> nickel (Ni), manganese (Mn) and aluminum (Al) have been incorporated into the layered structure to enhance the specific and residual capacity, rate performance, and structural stability,<sup>[4]</sup> to meet the high-capacity demands of next-generation batteries, especially solid-state batteries.<sup>[5]</sup>

Manganese rich oxides are considered to be high-voltage cathode materials ( $>4.5 \text{ V}$  versus  $\text{Li}/\text{Li}^+$ ), in layered and spinel<sup>[6]</sup> forms. Pure Li-manganese-oxides (LMO) in the form of  $\text{LiMnO}_2$  was found to be nonelectrochemically stable as it will irreversibly convert to spinel phases and result in loss of capacity, while Li-excess oxide  $\text{Li}(\text{Li}_{1/3}\text{Mn}_{2/3})\text{O}_2$  (also written as  $\text{Li}_2\text{MnO}_3$ ) suffers from structural change during the initial charging and degradation during subsequent cycling,<sup>[7]</sup> leading to capacity losses. It has been discovered that the inclusion of Ni and Co can benefit structures and capacity performances.<sup>[8]</sup> The combined layered form can be written in the form of  $[x \text{ Li}_2\text{MnO}_3(1-x) \text{ LiTMO}_2, \text{ TM} = \text{Mn, Ni, Co}]$ , consisting of both hexagonal *R-3m* structured, layered  $\text{LiTMO}_2$  and monoclinic  $\text{Li}_2\text{MnO}_3$  in the *C2/m* space group.  $\text{Li}_{1.2}\text{Mn}_{0.54}\text{Ni}_{0.13}\text{Co}_{0.13}\text{O}_2$  is one promising example of this type of cathode, with extensive research has been done to understand its mechanisms, to enhance the capacity performance, and improve the longevity.<sup>[9]</sup>

There have been multiple synthesis routes for this material, and the morphologies and electrochemical performances of

H. Li, M. B. Faheem, M. B. Saud, Y. Zhang, R. Qiao, P. Kaswekar, Q. Qiao  
Energy Conversion and Storage Laboratory

Department of Mechanical and Aerospace Engineering

Syracuse University

Syracuse 13244, NY, USA

E-mail: quqiao@syr.edu

B. Khan, J.-H. He

Department of Materials Science and Engineering

City University of Hong Kong

Kowloon 999077, Hong Kong

C. D. Rodmyre, P. Hauck, V. Kee, F. Zheng, A. L. Smirnova

Department of Chemistry Biology and Health Sciences South Dakota

School of Mines and Technology

Rapid City 57701, SD, USA

X. Wang, I. D. Hosein

Department of Biomedical and Chemical Engineering

Syracuse University

Syracuse 13244, NY, USA

 Supporting information for this article is available on the WWW under <https://doi.org/10.1002/batt.202500404>

 © 2025 The Author(s). *Batteries & Supercaps* published by Wiley-VCH GmbH. This is an open access article under the terms of the Creative Commons Attribution License, which permits use, distribution and reproduction in any medium, provided the original work is properly cited.

the final products can be different. These methods include coprecipitation, sol-gel, and solid-state synthesis methods. Coprecipitation has been a common method for preparing the precursor of layered oxide cathode materials in laboratory and commercial production. The traditional coprecipitation procedures are mostly carried out at mild temperatures ( $50\text{--}80\text{ }^{\circ}\text{C}$ ,<sup>[10]</sup>) but with extended time ( $>8\text{ h}$ ,<sup>[10b,11]</sup>), and multiple conditions are critical to the morphology of the precursor and the sintered product, including pH value,<sup>[12]</sup> temperature,<sup>[12b,13]</sup> and processing time.<sup>[13b]</sup> The spheres from the coprecipitation method are mostly secondary particles with diameters of micrometer range, consisting of numerous primary particles. Aside from spherical,<sup>[10a,11a,14]</sup> the morphology of the product can also be plates<sup>[15]</sup> from hydrothermal or solvothermal approaches, rods<sup>[15f,16]</sup> as obtained through the sol-gel method, and irregular shapes<sup>[15f]</sup> from solid-state methods. Novel morphologies have also been studied.<sup>[17]</sup> Aside from the material itself, electrolyte additives, doping, and surface engineering strategies<sup>[18]</sup> that lead to stable interfacial layers<sup>[11a,19]</sup> between electrodes and electrolytes and to stabilize the structures<sup>[20]</sup> have been extensively studied.

In this work, we are addressing the lengthy synthesis time factor and regulating crystalline dimensions by combining the microwave process with the introduction of a commercially available surfactant, sodium dodecyl sulfate (SDS), working in conjunction to achieve an accelerated process of cathode material preparation. The microwave irradiation significantly boosted the processing time of the precipitation progress from 8–10 h to 60 min, while the implementation of surfactant allowed a further accelerated step time of 15 min with comparable electrochemical performances and capacity retention. This process does not introduce organic chelating reagents to assist in morphology and element distribution, nor were electrolyte additives included.

## 2. Results

The synthesis procedure schematic is shown in Figure 1. The direct product from the microwave process displayed a faint pink color (experimental details are given in Supporting Information), with spherical morphology of 1–4  $\mu\text{m}$ . They were identified as transition metal carbonates  $\text{TMCO}_3$ <sup>[21]</sup> (Figure S1, Supporting Information) and subsequently sintered into oxides along with  $\text{Li}_2\text{CO}_3$ . The mixed carbonates were thoroughly dry-mixed prior to calcination.

### 2.1. Material Characterization

Thermal gravimetric analysis (TGA) was carried out on the precursor mixture to determine a suitable sintering temperature for the precursors. From Figure 2a, the mass loss between room temperature and 300°C can be attributed to the evaporation of absorbed water, taking up 2% of the initial mass. The loss of mass from 300 to 400 °C, 26% of the total initial mass, is from the decomposition of transition metal carbonates, releasing  $\text{CO}_2$ . During this phase,  $\text{NiCO}_3$  decomposes into  $\text{NiO}$ ,<sup>[22]</sup>  $\text{CoCO}_3$  is decomposed into  $\text{Co}_3\text{O}_4$  in the presence of oxygen,<sup>[23]</sup> and the decomposition of  $\text{MnCO}_3$  is also accompanied by the oxidation of Mn, forming  $\text{MnO}_2$  instead of  $\text{MnO}$  or  $\text{Mn}_2\text{O}_3$ .<sup>[24]</sup> The plateau between 400 and 600°C is attributed to the transition of transition metal oxides. Here, Ni and Co are further oxidized, forming oxides with +2 and +3 oxidation states, meanwhile  $\text{MnO}_2$  starts decomposition and forming oxides in lower oxidation states.<sup>[24]</sup> The slight change of mass can be attributed to the release of oxygen from Mn oxides and oxidation of Ni and Co. As Mn is higher in molar concentration, the mass balance tends toward reduction. When the temperature further increased, the reactions between the transition metal oxides and lithium carbonate were initiated.

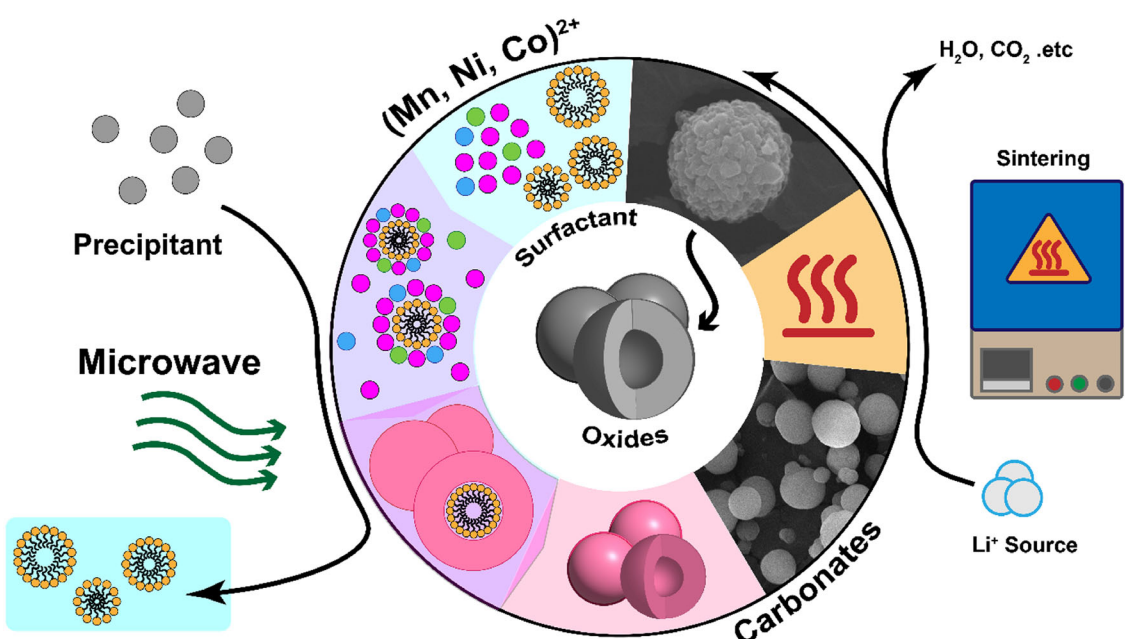
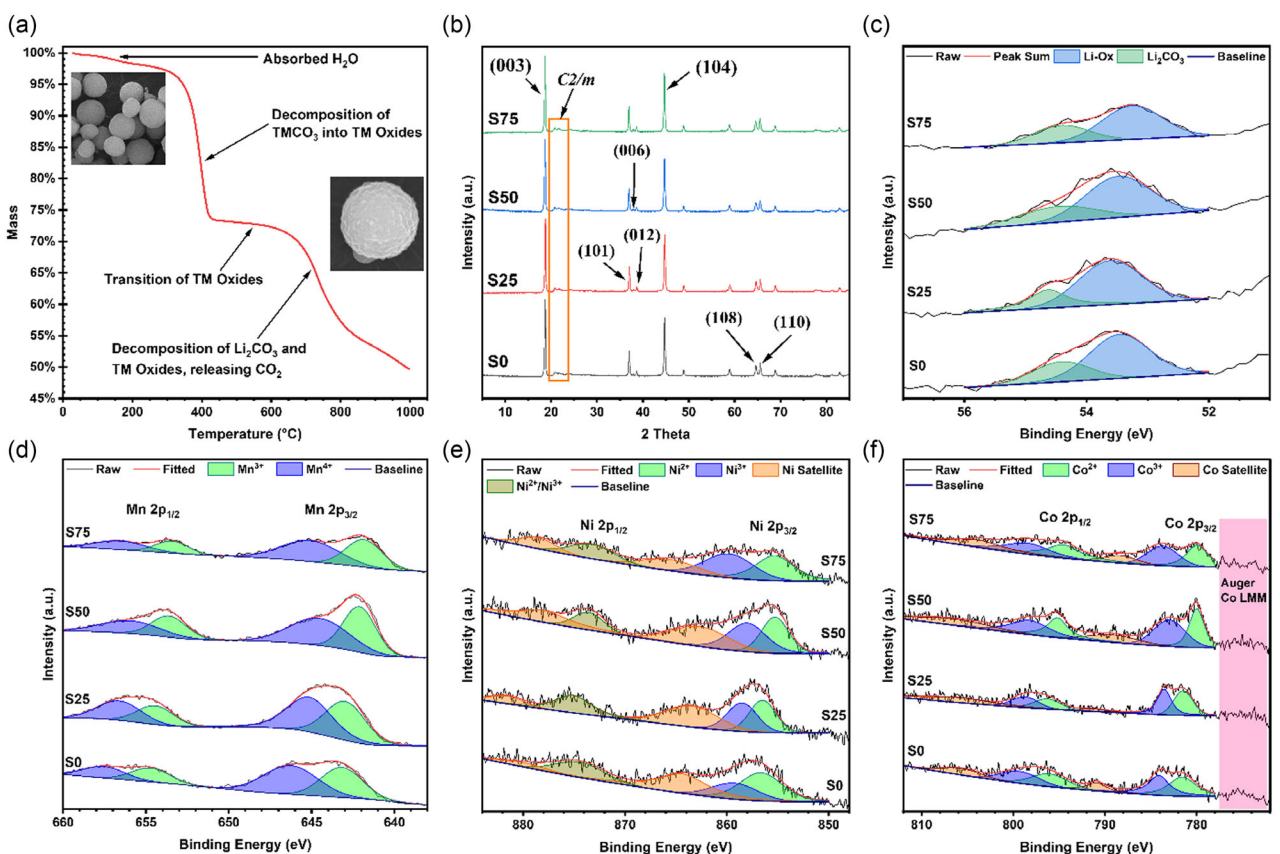


Figure 1. Process flow of microwave- and surfactant- assisted synthesis of Lithium–manganese-rich oxides (LMRO).



**Figure 2.** Thermal and X-ray analysis on the LMRO. a) Thermal gravimetric plot of microwave-synthesized LMRO, with insets of SEM imaging showing the morphologies; b) X-ray diffraction plots of sintered cathode materials; XPS of c) Li 1s, d) Mn 2p, e) Ni 2p, and f) Co 2p.

Since  $\text{Li}_2\text{CO}_3$  has a melting point of 723 °C, the reaction of oxides would be sufficient in a molten carbonate environment. The slope of loss in mass can be contributed by  $\text{Li}_2\text{CO}_3$ , as this phenomenon is not observed if  $\text{LiOH}$  is initially used as the lithium source.<sup>[25]</sup> Further increment of temperature can lead to significant loss of Li as seen in the gravimetric plot, and formation of Li-poor phases. Thus, the sintering temperature is set to 800°C for all the cathode materials in this study.

The X-ray diffraction patterns are shown in Figure 2b. The diffraction patterns of sintered samples suggest most peaks are in consistency of  $\alpha\text{-NaFeO}_2$ -structured, layered  $\text{LiTMo}_2$  crystalline (space group **R-3m**, TM = Mn, Ni, Co), indicating the presence of  $\text{LiMn}_{x}\text{Ni}_{y}\text{Co}_{(1-x-y)}\text{O}_2$ . The minor peaks present between 20°–25° can be identified as monoclinic  $\text{Li}_2\text{MnO}_3$  (space group **C2/m**), also called superlattice features. The presence of  $\text{Li}_2\text{MnO}_3$  indicates the Li-rich phase, with  $\text{LiMn}_6$  hexagonal layouts within the transition metal layer. The major peaks at 18° and 44° are attributed to two individual lattice planes, (003) and (104), the intensity ratio between these two peaks have been identified to indicate the degree of mixing of  $\text{Li}^+$  and TM cations, specifically disordering of  $\text{Ni}^{2+}$  due to the difference in their radii was minimal.<sup>[26]</sup> Table S1, Supporting Information, includes the  $\text{Ni}^{2+}$  mixing ratio from the refinement, and S50 has the lowest mixing among the samples. Other indications of layered oxide are the distinctive splitting of (006) and (012) peaks at 36°, also (108) and (110) at 65°.<sup>[27]</sup> The intensity ratios can be found in Table S1, Supporting

Information, and it can be observed that the intensity ratio of (003) and (104) ( $I_{003}/I_{104}$ ) was increasing with the surfactant concentration, reaching a maximum value for S50 and no increment when the surfactant concentration was further increased beyond. Similarly, the intensity ratio of summation of (006) and (012) over (101) also indicates the hexagonal ordering of the material, with S50 having the lowest value, its hexagonal ordering is the highest among them. Both ratios have been used to evaluate the layered structures.<sup>[27]</sup> The Rietveld refinement results and Figures are shown in Table S1, Supporting Information and Figure S3–S6, Supporting Information. Comparing these refinement results, all of them have similar lattice parameters, with similar  $c/a$  ratios, meanwhile S50 has the highest **R-3m** phase composition among all the experiment groups. The Raman spectroscopy also validated the presence of  $\text{LiTMo}_2$  and  $\text{Li}_2\text{MnO}_3$ <sup>[28]</sup> as shown in Figure S6, Supporting Information. The absence of other phases (i.e., spinel phases) hints that the distribution of lithium sources and carbonate precursors are even so the Li-poor phases are not formed in observable quantities. X-ray photoelectron spectra (XPS) analyzes were conducted over pristine and surfactant engineered composite, and the results of Li, Mn, Ni, and Co for pristine cathode materials are shown in Figure 2c–f, with C, O, and survey scans in Figure S8, Supporting Information. The C 1s spectra showed a peak at 289.8 eV, indicating the presence of carbonates, which can be attributed to  $\text{Li}_2\text{CO}_3$  formed on the surface after air exposure due to the residual  $\text{Li}_2\text{O}$  after sintering.  $\text{Li}_2\text{CO}_3$  was also determined

based on the Li 1s XPS spectra in Figure 2c. Surface residual Li oxides are also observed from the same spectra. The transition metal elements Mn, Ni, and Co spectra were also measured and shown in Figure 2d–f. The fitted profile of Mn indicates the highest molar ratio between  $Mn^{3+}$  and  $Mn^{4+}$  for pristine S50 (Table S2, Supporting Information). The presence of  $Mn^{4+}$  is mainly contributed by the  $Li_2MnO_3$  phase, in line with phase percentage determined from Rietveld refinement. Ni and Co spectra indicated that they were partially oxidized, with both +2 and +3 oxidation states post sintering. The average oxidation state of Ni increased from S0 to S50 and slightly decreased with further increasing of the surfactant concentration. The reduced percentage of  $Ni^{2+}$  is preferred due to the Li/Ni disorder, as mentioned in the diffraction section. The average oxidation of cobalt slightly increased with the addition of surfactant in the precursor solution and maintained stable with the increase in surfactant concentration. It can also be observed that the peak shifting of Mn 2p and Ni 2p toward lower binding energy with the increase of surfactant concentration. This phenomenon is in line with the average oxidation states of respective elements, also called chemical shift. The shift toward lower binding energy indicates a lower oxidation state. The presence of residual Na is in trace amount, as the Na 1s peak at 1071 eV and Na Auger peak at  $\approx$ 497 eV in survey scans (Figure S8, Supporting Information) are slightly visible, while the Na Auger KLL peak was not observed from the O 1s XPS spectra, nor can it be quantified from the EDS mapping. It can be deduced that the majority of SDS had been removed during the rinsing process. Also, there were no peaks appearing at  $\approx$ 1300 eV during the survey scans that can be attributed to Mg 1s which could originate from the sintering apparatus (MgO sintering boat) and not recognizable from the EDS mapping.

To observe the morphologies of the synthesized cathode materials, scanning electron microscope (SEM) images were obtained at various scales, as shown in Figure 3a–f and S2 and S9a–f, Supporting Information. The dimensions of secondary particles were similar between the control (S0) and the experimental groups S25–S75, and they all showed spherical morphologies stacked with primary particles. The primary particle size ranges from 50 to 600 nm, the size distribution charts of S0 and S50 are also shown in Figure 3g,h, with the distribution charts of S25 and S75 are shown in Figure S9, Supporting Information. It has been found that the decrease in primary particle size has positive effects on rate capabilities due to the shortened ion diffusion length.<sup>[12a,29]</sup> This is in line with the rate-capability results below. Energy dispersive spectroscopy mapping was also shown in Figure S10–S13, Supporting Information. The mapping showed uniform distribution of Mn, Ni and Co over the secondary particles. The ratios between the three elements were consistent with the initial ratios during preparation. Specifically, for S50, the oxygen atom concentration is slightly lower than the rest of the samples, meanwhile such concentration for S75 is higher. Focused ion beam (FIB) imaging revealed that the secondary particles were hollow, as shown in Figure S14, Supporting Information. The respective EDS element ratios are shown in S16–S19, Supporting Information. From the cross-section images of the secondary particles, S50 has a larger major vacancy inside, while the voids between primary particles is much less. Those tiny voids, visible in S0, S25, and S75, along with the main vacancies at

the center, contribute to the difference in specific surface area (Figure S15, Supporting Information). S50 is measured with highest specific surface area from its large vacancy inside, while S0 and S75, with similar surface area values, are contributed by their primary particle voids. S25 exhibited the lowest specific surface area as it had a smaller central vacancy and the absence of voids among primary particle stacking. The specific surface area values will be further used in calculating the ion diffusion rate below.

The effect of surfactant presence can be discussed as such: Most surfactants consist of a hydrophilic head and a hydrophobic end. Under a fixed temperature, when the concentration of a surfactant in a solvent is beyond the critical micelle concentration (CMC), spheres containing a fixed amount (aggregation number) of surfactant molecules will start to form, named as micelles. For SDS dissolved in water at 25 °C, the CMC is 8.2 mM, and the aggregation number under this condition is 62–64,<sup>[30]</sup> with a micelle size of  $\approx$ 1.8 Å.<sup>[31]</sup> The actual aggregation numbers and micelle sizes could vary as the addition of salts and ethanol. The uniformity of the micelle size can regulate the seed formation of primary particles, resulting in a narrow crystalline size distribution.<sup>[32]</sup> During the microwave heating process, the carbonate primary particles packed into secondary particles and their sizes are uniformed under Oswald ripening.<sup>[10b]</sup> This resulted in a narrow size distribution of the primary particles shown in insets of Figure 3c, f and S9g–h, Supporting Information. To be noted that the size of micelles is temperature dependent thus the size regulating is not as significant as in the seed formation process. However, within this study, excessive concentrations of SDS surfactants do not lead to uniform secondary particle morphologies. In Figure S20, Supporting Information, the spherical shape is not recognizable when the SDS concentration is increased to 15 times of the CMC, or S150 under the nomenclature mentioned in the experimental section in Supporting Information, while for S100, the spherical morphologies still retain. The secondary particles remained hollow for both high concentrations of surfactant involved. Specific surface area is also decreasing following the further increase of the surfactant concentration. Also, the surfactants can affect the crystal growth orientation.<sup>[4a]</sup> Since it has been previously discovered that the presence of ethanol during the precursor crystallization process can have effects of preferred direction of crystal growth,<sup>[33]</sup> thus the concentration of ethanol has been maintained for all cathode materials synthesized within this study. The transmission electron microscope images (Figure 3i–l) indicate the presence of layered structures of  $Li_2MnO_3$  and  $LiTMO_2$ , as the distances between atom layers of 0.473 nm (Figure 3 h,j) can be attributed to the spacing of (003) planes in the rhombohedral  $R\text{-}3m$  phase and the spacing between (001) planes within the monoclinic  $C2/m$  phase, respectively. These values were close to the calculated ones from the Rietveld refinements and were not affected by the introduction of the surfactant during the intermediate synthesis process.

## 2.2. Electrochemical Performance

To study the effectiveness of microwave assistance in terms of accelerating the precipitation process, a cyclic voltammetry

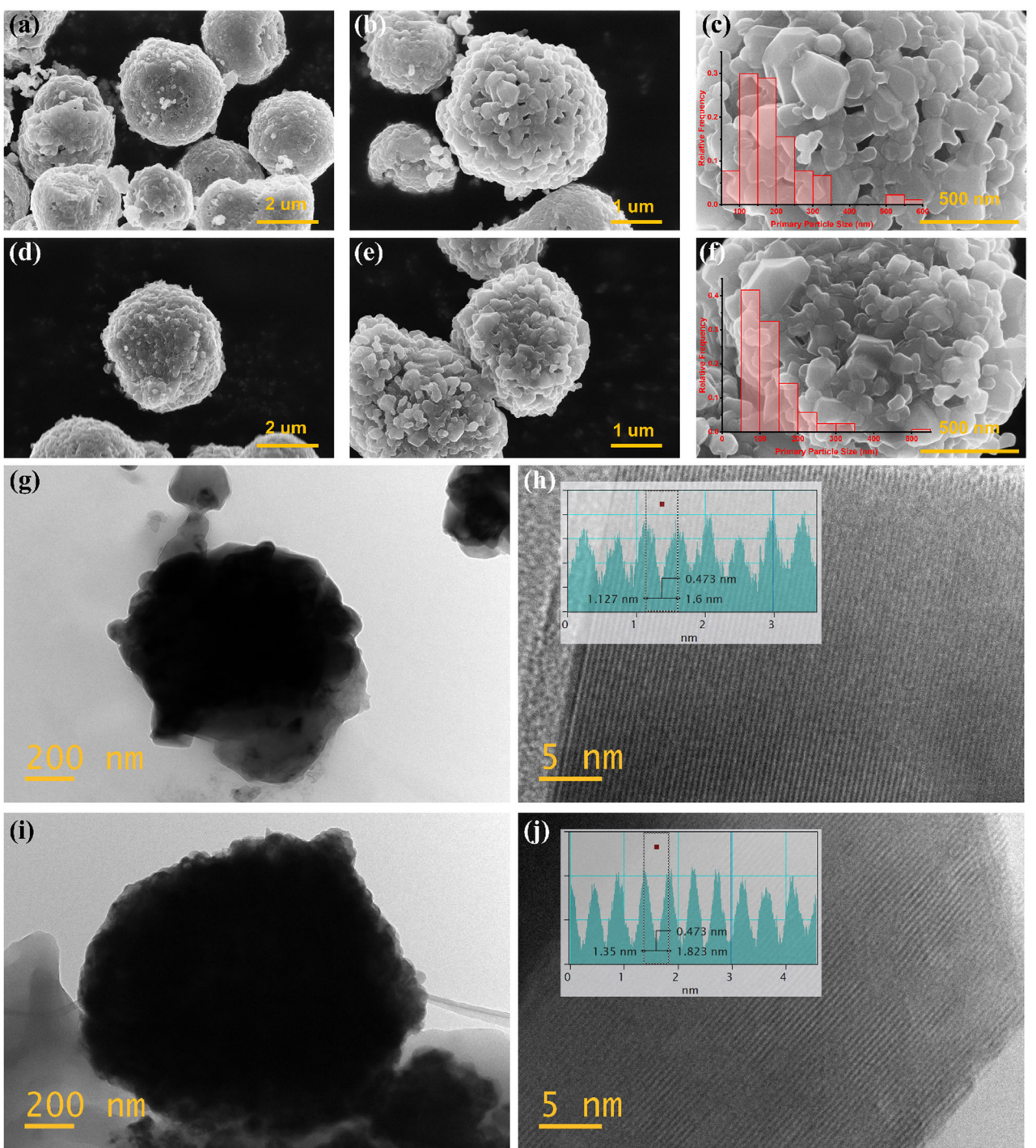


**Figure 3.** Microscopic characterization of LMRO. Scanning electron microscopic images of a–c) S0, d–f) S50 with primary particle size distributions in (c) and (f), respectively; transmission electron microscopic images of g,h) S0, and i,j) S50 with insets showing the spacing of layered structures.

(CV) was employed initially to observe the redox potentials of the cathode material synthesized under a 60-min microwave profile (**Figure 4a**). The CV plot shows the initial oxidation peak at 4.3 V and the activation of  $\text{Li}_2\text{MnO}_3$  above 4.5 V. This activation involves the oxidation of lattice oxygen atoms.<sup>[14b]</sup> It can be seen from the same plot; the activation reaction is incomplete during the initial charge process, as the oxidation peak at 4.65 V is visible in the second charging cycle. The reduction peak at 3.7 V shifts toward

lower potential. The effects of surfactant concentrations on actual electrochemical cell performance are evaluated by charge-discharge cycling, along with electrochemical impedance spectroscopy. During the initial charging setup (**Figure S21**, Supporting Information),  $\text{Li}_2\text{MnO}_3$  is seen activated beyond 4.4 V versus Li/Li<sup>+</sup>, showed as a “plateau” feature in the initial charging curve between 4.45 and 4.65 V. This matches the oxidation peak at 4.65 V during the first cycle in the CV plot. The second charging

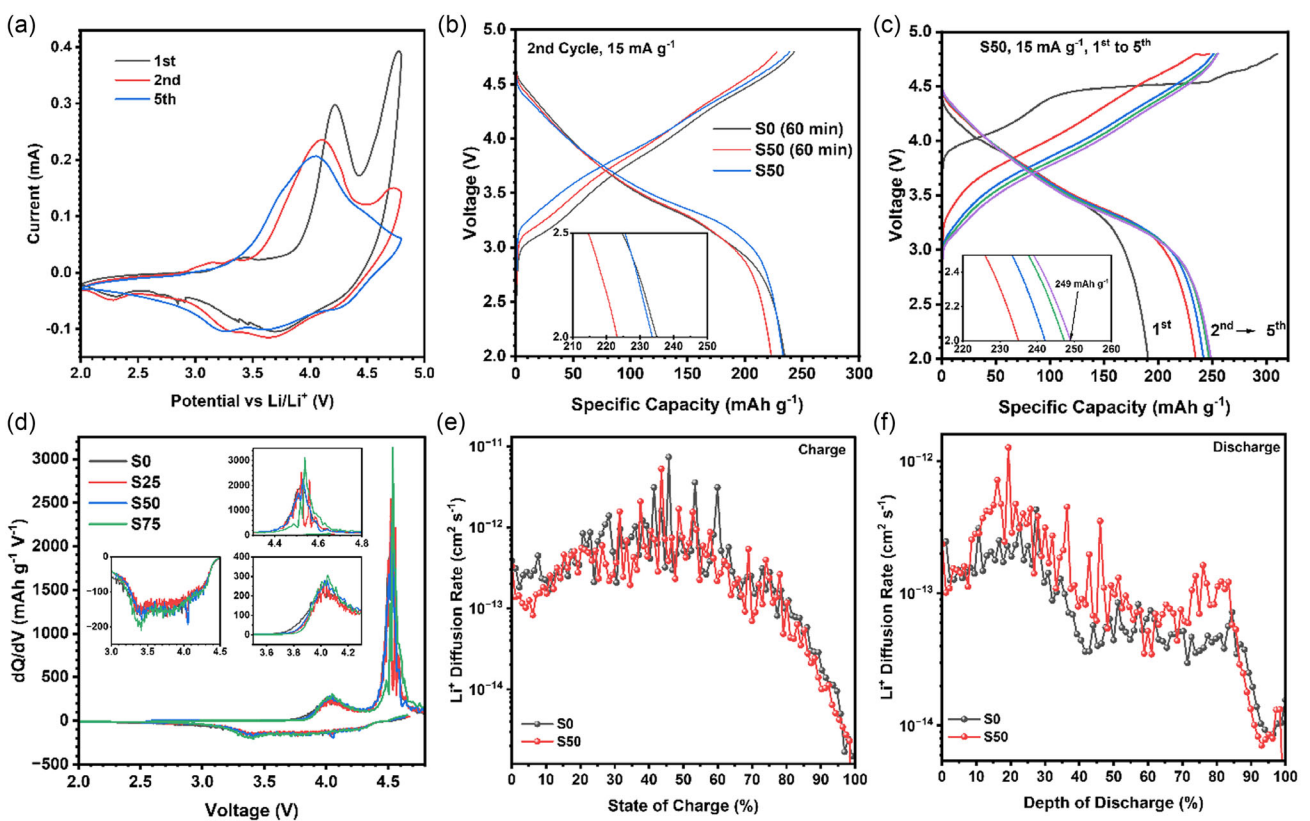


**Figure 4.** Electrochemical performances and analysis of LMRO. a) CV graph of S0 (60 min); b) Capacity–voltage profile comparison of 60 min and 15 min; c) dQ/dV plot of the initial cycles; d) Capacity–voltage profile of initial charge–discharge cycles, S50; and Li<sup>+</sup> Diffusion rates at 15 mA g<sup>-1</sup>; e) Charging, and f) discharging.

process also displayed a small plateau close to cutoff threshold and can be matched with the residual oxidation peak in CV plot. The dQ/dV plot of the initial cycle, shown in Figure 4d, also indicates the presence of peaks at 4.5–4.6 V. The peaks position and area are similar and are not strongly correlated with the concentration of surfactant, which indicates that the addition of surfactant does not alter the key electrochemical redox reactions. The electrochemical impedance spectroscopic plots (Figure S22, Supporting Information) of S0 to S75 were fitted, and the fitting results showed that the charge transfer resistance of S50 is the lowest among the groups, also that S50 has lower bulk and diffusion resistances than the materials prepared with other surfactant concentrations (Table S3, Supporting Information). The voltage–capacity plots of postformation cycles at 15 mA g<sup>-1</sup> indicate that the specific capacity is higher for the cathode material synthesized with 5 CMC of SDS at 60-min MW processing, as shown in Figure 4b. The time reduction optimization was carried out, and the results shown in Figure 4b showed that the 15-min processed cathodes with the same surfactant concentration yielded similar capacity performances starting from the second cycle. The initial cycle shown in Figure S21, Supporting Information, shows that in the case of 15-min microwave profile, the inclusion of surfactant yielded in slightly higher capacity performances, while in the case of 60-min microwave profile, the addition of surfactant did not show advantage over the control batch. The inferior performance with the combination of

surfactant and extended time can be due to the excessive crystalline size. The area underneath the discharge curve is also higher, indicating an increased specific energy. A specific capacity of 249 mAh g<sup>-1</sup> was measured at 15 mA g<sup>-1</sup> during the 5th cycle, as shown in Figure 4c with a specific energy of 865 Wh kg<sup>-1</sup>.

Rate-capability test was carried out to examine the performance of the cathodes at various current densities. From Figure 5a, it can be clearly observed that the specific capacities at various charge–discharge rates and the capacity retention for S50 were higher compared to the rest of the surfactant concentration groups. The specific capacity at 600 mA g<sup>-1</sup> is 143 mAh g<sup>-1</sup>. S25 exhibited low specific capacities at all current density levels, and S75 showed similar specific capacities to that of S50 of up to 60 mA g<sup>-1</sup>. It is also observed that under increasing current densities, specific capacity of S75 drops rapidly, and to that of 1500 mA g<sup>-1</sup>, both S25 and S75 did not show usable capacity. This hints that the diffusion rate of Li<sup>+</sup> could be the limiting factor. As shown in the electrochemical impedance spectroscopy (EIS) fitting values, the diffusion resistance of precycling materials already shows some difference. The ohmic overpotential can allow voltage reaching the threshold prior to ion diffusive equilibrium, resulting in false capacities. To understand the different rate–capacity performance behaviors, galvanostatic intermittent titration technique (GITT) was employed to determine the diffusion rate of lithium ion,  $D_{Li^+}$ .

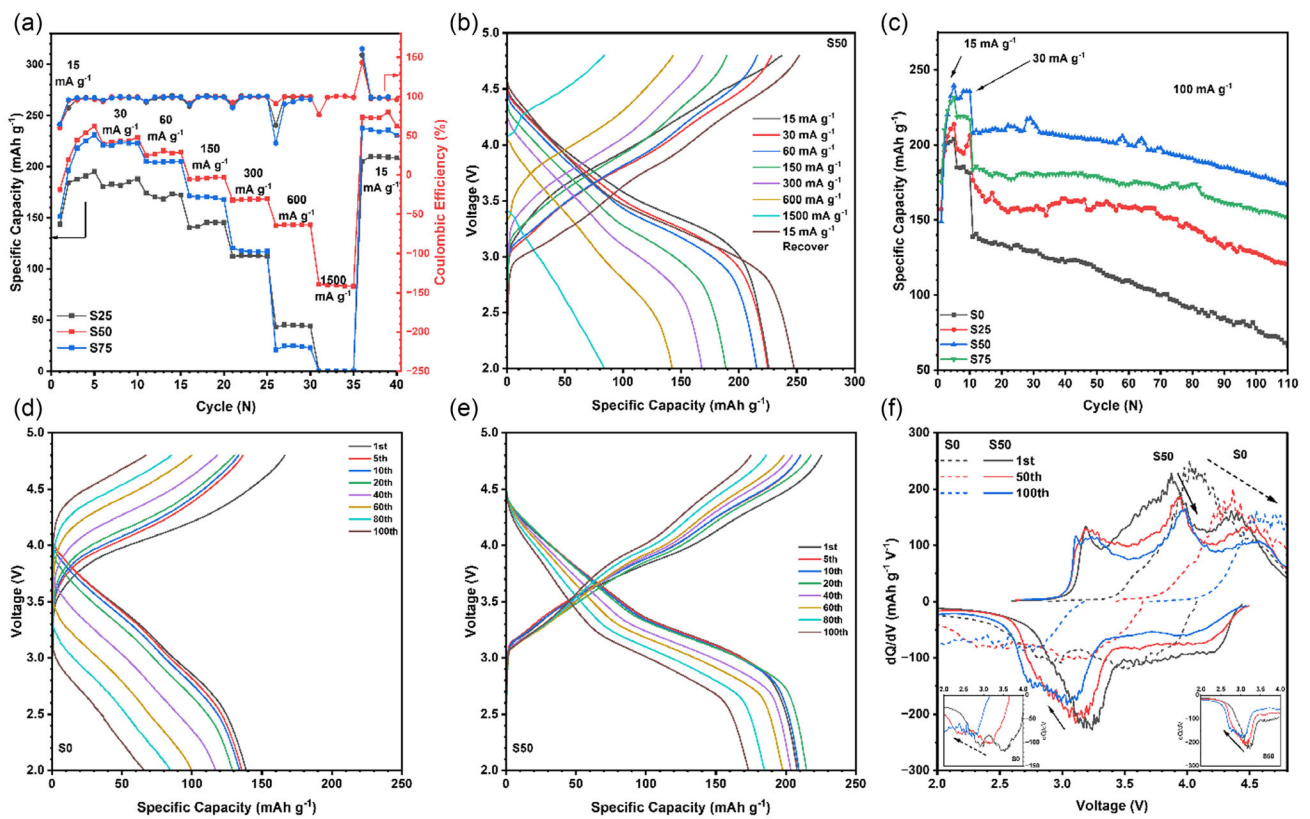


**Figure 5.** a) Rate-capacity performances of the cathodes, with charge–discharge capacity–voltage profiles of S50 in b); c) long-term capacity retention of S0, S25, S50, and S75 at  $100 \text{ mA g}^{-1}$ ; capacity–voltage curves of d) S0 and e) S50; and f) cycling  $dQ/dV$  plots for S0 and S50 under  $100 \text{ mA g}^{-1}$ , with insets showing charge/discharging peak shifts and intensity fading.

Equation (1) is used to calculate the diffusion rate<sup>[34]</sup>:

$$D_{Li^+} = \frac{4}{\pi} \left( \frac{V \Delta E_{OC}/\Delta t_i}{A dE/d\sqrt{t}} \right)^2 \quad (1)$$

Here,  $V$  is the molar volume calculated from the lattice parameters obtained from Rietveld refinement,  $A$  is the specific surface area measured via BET physisorption,  $\Delta E_{OC}$  is the difference in open circuit potential,  $\Delta t_i$  is the time elapsed when a constant current is applied between  $E_{OC}$  measurements,  $E$  stands for the electrode potential, and  $t$  is the step time (pulse). The voltage–time plots are shown in Figure S23, Supporting Information, and a reduced internal ohmic potential can be observed for S50. As shown in Figure 4e,f, during charging, both S0 and S50 have their  $\text{Li}^+$  diffusion coefficients ranging between  $10^{-13}$  and  $10^{-12} \text{ cm}^2 \text{ s}^{-1}$  from 0%–80% state of charge. And during discharging, S50 exhibited higher diffusion coefficient within  $10^{-13}$ – $10^{-12} \text{ cm}^2 \text{ s}^{-1}$  at 5%–80% depth of discharge over S0. This is in line with the fitted EIS plots regarding the fitted diffusion resistance. The increment of diffusion rate could be attributed to the orientation of crystalline growth. With the concentration of ethanol being a fixed parameter, this change of growth orientation can be attributed to the directing effect of surfactant.<sup>[4a]</sup> This can also be correlated with the  $R\text{-}3m$  phase percentage as obtained by Rietveld refinement.

The capacity decay of 100 cycles under  $100 \text{ mA g}^{-1}$  of S50 is also the lowest among all the groups, with 83.89% of capacity retained, as shown in Figure 5c, meanwhile, it was observed that

S0 retained less than half of its initial capacity (47.49%) at the beginning of  $100 \text{ mA g}^{-1}$  tests. Respective charge–discharge capacity–voltage profiles of selective cycles under  $100 \text{ mA g}^{-1}$  of S0 and S50 are shown in Figure 5d,e, with S25 and S75 shown in Figure S24, Supporting Information. The voltage decay for S50 is also significantly lower than that of S0, with 0.2477 V versus 0.6831 V over the 100 cycles, as shown in Figure S25, Supporting Information. A  $dQ/dV$  plot comparing the profiles of S0 and S50 at certain cycles is shown in Figure 5f, with detailed  $dQ/dV$  plots including S25 and S75 are shown in Figure S26, Supporting Information. The peak and intensity shift of S50 is less than those of S0 after 100 cycles, indicating a significantly reduced amount of loss in cyclable lithium ions and redox pairs, while the peaks are completely shifted and deformed in the case of S0, in correlation with the drastic capacity and voltage decay meaning the amount of accessible redox pairs is reduced. In S75, the discharge  $dQ/dV$  profile has less drift than S25 and S0 from the 1st cycle to the 50th cycle and less peak shifting and area reduction than S25 in both charge and discharge profiles.

To further understand the difference in terms of capacity retention and voltage decay, postcycling analysis was performed for S0 and S50 to examine the changes in morphology and structure that result in the difference in capacity retention. The postcycling SEM and XPS spectra of S50 were shown in Figure 6. The macroscopic morphology changes in the postcycling S50 were minimal, the spherical morphology remained, with no visible cracks observed on the external surfaces. Additionally,

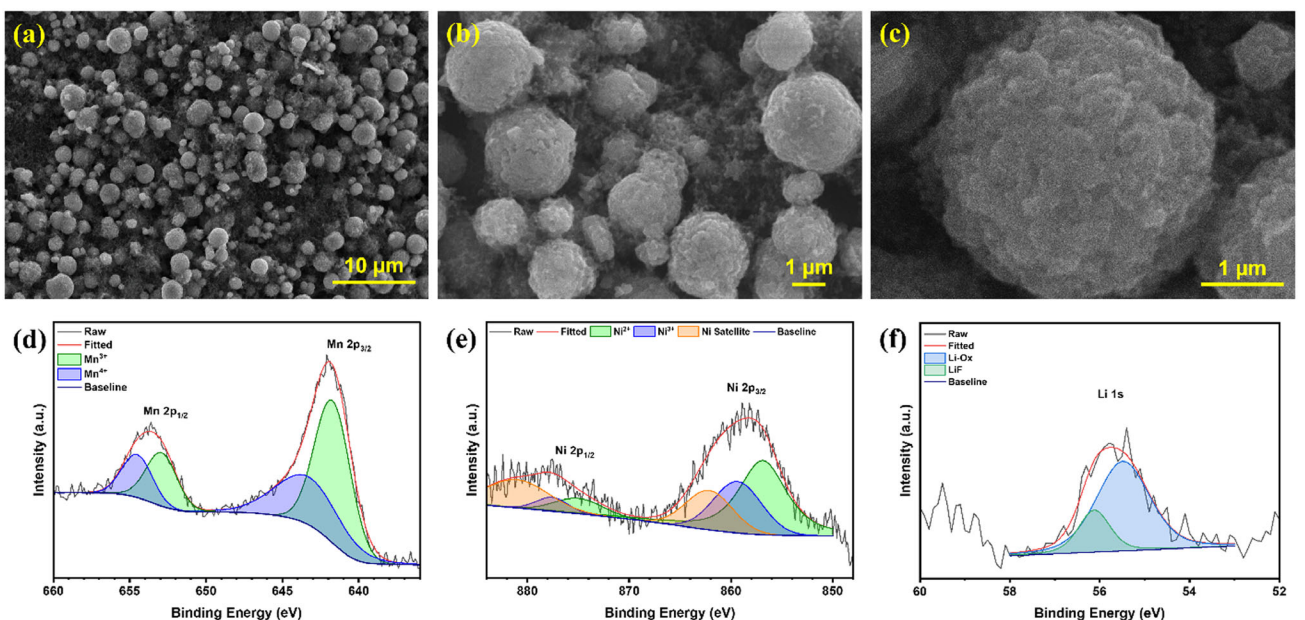


**Figure 6.** Postcycling analysis of LMRO. a–c): SEM of S50 after 100 cycles under  $100 \text{ mA g}^{-1}$  and d–f): Mn 2p, Ni 2p, and Li 1s XPS spectra of postcycling S50.

cross-section images of postcycling S0 and S50 were obtained through FIB, as seen in Figure S27, Supporting Information. In both cathodes, the hollow spheres were not collapsed. However, the external primary particles are seen detaching as a shell from the inner sphere in the case of S0; while in S50, the cross-section revealed visible grain boundaries. The increased concentration of Mn<sup>4+</sup> after cycling in S50 can be attributed to the Li-poor Li-Mn oxides, that is,  $\text{LiMn}_2\text{O}_4$ ,  $\text{Li}_4\text{Mn}_5\text{O}_{12}$  spinel phases. The formation of such phases may induce the formation and propagation of the boundaries present in the FIB image. For S0 after the 100 cycles at  $100 \text{ mA g}^{-1}$ , the photoelectron spectra of Mn and Co were not obtained (Figure S25, Supporting Information). This matches the disappearance of oxidation and reduction peaks within the corresponding voltage window, for example, the Mn<sup>3+</sup>/Mn<sup>4+</sup> redox pair at  $\approx 2.7 \text{ V}$  during discharge,<sup>[35]</sup> from the dQ/dV plots shown in Figure 5f and S24, Supporting Information. This loss of element spectra can be associated with the significant capacity drop, as they could have been dissolved near the surface or buried underneath Nickel compounds due to the drifting of Ni<sup>2+</sup>, resulting in loss of accessible redox pairs. The survey scan also showed the presence of P from the peak at  $\approx 135 \text{ eV}$  for both electrodes, which could be either coming from the residual LiPF<sub>6</sub> salt or its degradation products.

### 3. Conclusion

The inclusion of SDS surfactant and microwave processing in the synthesis process of lithium–manganese-rich oxide cathode proves to yield a similar capacity performance with reduced processing time, while the standalone conditions were found to be inferior in electrochemical performance. The optimal condition obtained from this study is that the concentration of SDS surfactant at 5 CMC in combination with 15 min of microwave

processing at  $170^\circ\text{C}$ . Microwave processing of the intermediate product significantly reduced time consumption. Under low current densities, it can reach  $\approx 249 \text{ mAh g}^{-1}$  and under elevated charging/discharging rates,  $143 \text{ mAh g}^{-1}$  at  $600 \text{ mA g}^{-1}$ . Adding the surfactant yielded a slightly higher percentage of rhombohedral *R-3m* phase, as it can provide regulation on the orientation of crystalline growth. This results in improved lithium-ion diffusion rate, which promotes rate-capacity performances. The capacity retention also benefits from the inclusion of SDS surfactant under the boosted synthesis. The accelerated process achieved by both microwave and SDS surfactant can be a viable approach to increase the production rate of such cathode materials.

## 4. Experimental Section

### Material Synthesis

Sodium Dodecyl Sulfate (SDS, Thermo Scientific) was dissolved in DI water and labeled as A.  $\text{MnSO}_4 \cdot \text{H}_2\text{O}$ ,  $\text{NiSO}_4 \cdot 6\text{H}_2\text{O}$ ,  $\text{CoSO}_4 \cdot 7\text{H}_2\text{O}$  (Sigma-Aldrich) were dissolved in deionized water with molar ratio of 4:1:1 and stirred for 15 min, then added into A. Ammonium bicarbonate (Sigma-Aldrich) was dissolved in water and stirred for 15 min at room temperature, an equal volume of ethyl alcohol was added to form a cloudy suspension B. B was added to A under stirring, forming a light-purple suspension. This mixture was then microwave-processed (Anton-Paar MonoWave 450) for 15 or 60 min at  $170^\circ\text{C}$  under stirring and subsequently quenched with compressed air. The internal pressure reading during microwave soaking was 15 bars. The precipitate was then separated from the supernatant and rinsed with water and ethyl alcohol (Acros Organics) and dried at  $80^\circ\text{C}$  under vacuum for 12 h. The dried precursor was subsequently mixed thoroughly with  $\text{Li}_2\text{CO}_3$  (Sigma-Aldrich) using a high-speed mixer (Flacktek DAC 330-100 PRO), presintered at  $500^\circ\text{C}$  for 5 h followed by  $800^\circ\text{C}$  for 12 h in air, with a heating ramp of  $2^\circ\text{C min}^{-1}$ . Based on the concentration of SDS in the precursor solution, the cathode samples are labeled as S0, S25, S50, and S75 for 15-min microwave processing, where 25, 50, and 75 are referred to the multiplier of CMC

(i.e., S50 = 5 CMC) prior to mixing with precipitant. S0 (60 min) and S50 (60 min) were investigated at the start of this study, with 60 min of MW processing time.

## Material Characterizations

The synthesized cathode precursors underwent TGA with a Q500 TGA (TA Instruments) scanned from room temperature to 1000 °C at 5 °Cmin<sup>-1</sup>. Powder X-ray diffraction was carried out with a Rigaku Miniflex 600 diffractometer (Cu K $\alpha$ ) from 5° to 85° with a step width of 0.02°. The diffraction data was refined with GSAS-II software suite. The sintered cathodes were observed under SEM (JEOL IT-100), field-emission SEM (Thermo Fisher Scientific Helios 5-CX, with FIB), and transmission electron microscope (JEOL JEM-2100). Ex situ Raman spectra were obtained via a Renishaw InVia confocal Raman microscope equipped with 532 nm laser. XPS were obtained from Thermo Fisher ESCALAB XI<sup>+</sup> system, with an Al K $\alpha$  (1486.7 eV) monochromatic X-ray source and a 16-channel detector, were used to determine the composition and valance states of constituent elements. The pass energy for the survey scans was 187.5 eV (200 m spot size). The high-resolution core-level scans used a pass energy of 23.5 eV, and the XPS binding energy was calibrated using the N 1s peak as a reference. The XPS peak 4.1 software was used to analyze the XPS peaks. Background corrections Shirley + Linear and Tougaard + Linear were used. The surface area of the cathode samples was obtained through Micromeritics Gemini 2375 using Brunauer–Emmett–Teller theory.

## Electrochemical Characterizations

The as-synthesized cathode materials were premixed with poly(vinylidene fluoride) (PVDF, Sigma-Aldrich) and Super P (Alfa Aesar) in a mass ratio of 80:10:10 and then dispersed in *N*-methyl-2-pyrrolidone (NMP, Sigma-Aldrich) under rapid mixing (Flacktek DAC 330-100 PRO) under room temperature. The mixture was subsequently blade-casted at 55 °C on a 15 μm aluminum foil, followed by vacuum drying at 80 °C overnight. The dried cathodes were punched into 12 mm dishes (active material loading ≈2.7 mg cm<sup>-2</sup>) and assembled into CR2032 coin batteries using φ15.6 × 0.25 mm lithium metal (MTI Corps) as the anode, Celgard 2500 as the separator, and 1 M LiPF<sub>6</sub> in EC/EMC v/v 3:7 (MTI Corps) as the liquid electrolyte. The assembly of batteries was carried out in an argon-filled glovebox (MTI Corps) with moisture and oxygen contents maintained below 0.1 ppm.

EIS and CV were carried out using a BioLogic SP-150 Potentiostat. Charge-discharge tests and GITT were carried out with Landt CT2001A battery testers. The electrochemical tests and charge-discharge tests were carried out at a room temperature of 21 °C.

## Acknowledgements

This work is supported by Syracuse University and NSF IUCRC Center for Solid-State Electric Power Storage (CEPS) grant no. (2052611).

## Conflict of Interest

The authors declare no conflict of interest.

## Author Contributions

**Hansheng Li:** design of project; experimental executions; data analyses; conceptualization; writing, reviewing. **M. Bilal Faheem:**

conceptualization; analyses; writing, reviewing. **Madan Bahadur Saud:** analyses; writing, reviewing; conceptualization. **Bilawal Khan:** XPS analyses; reviewing. **Yuchen Zhang:** writing, reviewing; conceptualization. **Collin D. Rodmyre:** SEM, FIB, TEM analyses; reviewing. **Ruosi Qiao:** reviewing; electrochemical performance analyses. **Xinlu Wang:** Raman spectroscopy; TGA, reviewing. **Phillip Hauck:** BET, TEM analyses; reviewing. **Vanessa Kee:** TEM analyses; reviewing. **Poojan Kaswekar:** reviewing. **Fan Zheng:** SEM, FIB, TEM analyses; reviewing. **Ian Dean Hosein:** Raman spectroscopy; reviewing. **Jr-Hau He:** XPS analyses; reviewing. **Alevtina L. Smirnova:** conceptualization; data analyses; writing; reviewing. **Quinn Qiao:** conceptualization; data analyses; writing, reviewing.

## Data Availability Statement

The data that support the findings of this study are available from the corresponding author upon reasonable request.

**Keywords:** layered lithium-rich cathodes · microwave synthesis · surfactant engineering

- [1] a) N. Liu, L. Hu, M. T. McDowell, A. Jackson, Y. Cui, *Acs Nano* **2011**, *5*, 6487; b) G. Zheng, S. W. Lee, Z. Liang, H. W. Lee, K. Yan, H. Yao, H. Wang, W. Li, S. Chu, Y. Cui, *Nat. Nanotechnol.* **2014**, *9*, 618; c) J. Zheng, H. Zheng, R. Wang, L. Ben, W. Lu, L. Chen, L. Chen, H. Li, *Phys. Chem. Chem. Phys.* **2014**, *16*, 13229; d) J. Liu, Q. Zhang, T. Zhang, J.-T. Li, L. Huang, S.-G. Sun, *Adv. Funct. Mater.* **2015**, *25*, 3599.
- [2] a) K. Mizushima, P. C. Jones, P. J. Wiseman, J. B. Goodenough, *Mater. Res. Bull.* **1980**, *15*, 783; b) N. A. Godshall, I. D. Raistrick, R. A. Huggins, *Mater. Res. Bull.* **1980**, *15*, 561.
- [3] K. Ozawa, *Solid State Ionics* **1994**, *69*, 212.
- [4] a) X. Ju, H. Huang, W. He, H. Zheng, P. Deng, S. Li, B. Qu, T. Wang, *ACS Sustain. Chem. Eng.* **2018**, *6*, 6312; b) X. Li, M. Liang, J. Sheng, D. Song, H. Zhang, X. Shi, L. Zhang, *Energy Storage Mater.* **2019**, *18*, 100; c) K.-J. Park, J.-Y. Hwang, H.-H. Ryu, F. Maglia, S.-J. Kim, P. Lamp, C. S. Yoon, Y.-K. Sun, *ACS Energy Lett.* **2019**, *4*, 1394; d) X. Li, L. Jin, D. Song, H. Zhang, X. Shi, Z. Wang, L. Zhang, L. Zhu, *J. Energy Chem.* **2020**, *40*, 39; e) F. X. Xin, A. Goel, X. B. Chen, H. Zhou, J. M. Bai, S. Z. Liu, F. Wang, G. W. Zhou, M. S. Whittingham, *Chem. Mater.* **2022**, *34*, 7858; f) H. B. Lee, T. Dinh Hoang, Y. S. Byeon, H. Jung, J. Moon, M. S. Park, *ACS Appl. Mater. Interfaces* **2022**, *14*, 2731; g) J. Jeyakumar, Y.-S. Wu, S.-H. Wu, R. Jose, C.-C. Yang, *ACS Appl. Energy Mater.* **2022**, *5*, 4796; h) S. Cangaz, F. Hippauf, R. Takata, F. Schmidt, S. Dörfler, S. Kaskel, *Batter. Supercaps* **2022**, *5*, e202200100; i) Y. Shin, S. Maeng, Y. Chung, G. K. Krumdick, S. Min, *Small* **2021**, *17*, e2100040.
- [5] a) K. Gao, C. Sun, Z. Wang, *Mater. Chem. Front.* **2024**, *8*, 3082; b) F. Bahmani, A. W. Smirnova, *J. Mater. Chem. A* **2025**, *13*, 18732; c) F. Bahmani, C. Rodmyre, K. Ly, P. Mack, A. W. Smirnova, *Batter.-Basel* **2024**, 10.
- [6] M. M. Thackeray, W. I. F. David, P. G. Bruce, J. B. Goodenough, *Mater. Res. Bull.* **1983**, *18*, 461.
- [7] a) J. Rana, M. Stan, R. Kloepsch, J. Li, G. Schumacher, E. Welter, I. Zizak, J. Banhart, M. Winter, *Adv. Energy Mater.* **2014**, *4*; b) P. Yan, L. Xiao, J. Zheng, Y. Zhou, Y. He, X. Zu, S. X. Mao, J. Xiao, F. Gao, J.-G. Zhang, C.-M. Wang, *Chem. Mater.* **2015**, *27*, 975.
- [8] W. Huang, C. Lin, M. Zhang, S. Li, Z. Chen, W. Zhao, C. Zhu, Q. Zhao, H. Chen, F. Pan, *Adv. Energy Mater.* **2021**, *11*, 2102646.
- [9] a) E. Hu, X. Yu, R. Lin, X. Bi, J. Lu, S. Bak, K.-W. Nam, H. L. Xin, C. Jaye, D. A. Fischer, K. Amine, X.-Q. Yang, *Nat. Energy* **2018**, *3*, 690; b) X. Li, K. Zhang, D. Mitlin, Z. Yang, M. Wang, Y. Tang, F. Jiang, Y. Du, J. Zheng, *Chem. Mater.* **2018**, *30*, 2566; c) P. K. Nayak, L. Yang, K. Pollok, F. Langenhorst, D. Aurbach, P. Adelhelm, *ChemElectroChem* **2019**, *6*, 2812; d) W. He, P. Liu, B. Qu, Z. Zheng, H. Zheng, P. Deng, P. Li, S. Li, H. Huang, L. Wang, Q. Xie, D. L. Peng, *Adv. Sci. Weinh.* **2019**, *6*, 1802114; e) J. Hwang, S. Myeong, W. Jin, H. Jang, G. Nam, M. Yoon, S. H. Kim, S. H. Joo, S. K. Kwak, M. G. Kim, J. Cho, *Adv. Mater.*

- [2020, 32, e2001944; f) Z. Li, Q. Li, S. Wu, A. Zhang, H. Zhuo, G. Zhang, Z. Wang, L. Wang, Z. Ren, J. Wang, *ChemistrySelect* 2020, 5, 3052; g) Z. Zhao, M. Sun, T. Wu, J. Zhang, P. Wang, L. Zhang, C. Yang, C. Peng, H. Lu, *Nanomicro Lett.* 2021, 13, 118; h) J. Hwang, S. Myeong, E. Lee, H. Jang, M. Yoon, H. Cha, J. Sung, M. G. Kim, D.-H. Seo, J. Cho, *Adv. Mater.* 2021, 33, 2100352; i) Z. H. Guo, L. Li, Z. H. Su, G. C. Peng, M. Z. Qu, Y. X. Fu, H. Wang, W. J. Ge, *Electrochim. Acta* 2023, 437.
- [10] a) B. Qiu, C. Yin, Y. Xia, Z. Liu, *ACS Appl. Mater. Interfaces* 2017, 9, 3661; b) L. Lu, Y. Hu, H. Jiang, C. Zhu, J. Chen, C. Li, *ACS Appl. Mater. Interfaces* 2019, 11, 25796.
- [11] a) Z. Xiao, J. Liu, G. Fan, M. Yu, J. Liu, X. Gou, M. Yuan, F. Cheng, *Mater. Chem. Front.* 2020, 4, 1689; b) J. Li, R. Doig, H. S. Liu, G. Botton, J. R. Dahn, *J. Electrochem. Soc.* 2016, 163, A2841.
- [12] a) J. Y. Park, J. Choi, S. Lee, J. S. Jeong, K. S. Min, J. S. Lee, H. Kim, J. S. Park, J. Park, S. Yoon, *ACS Appl. Mater. Interfaces* 2024, 16, 22048; b) J. Zheng, M. Gu, A. Genc, J. Xiao, P. Xu, X. Chen, Z. Zhu, W. Zhao, L. Pullan, C. Wang, J. G. Zhang, *Nano Lett.* 2014, 14, 2628; c) B. Hu, X. B. Lou, C. Li, F. S. Geng, M. C. Yang, M. Shen, B. W. Hu, *Chemelectrochem* 2019, 6, 1385.
- [13] a) F. G. Yu, J. X. Nong, Z. G. Zou, M. Feng, S. C. Zhang, F. G. Liang, S. K. Jia, M. Chen, *J. Energy Storage* 2024, 98; b) Y. H. Xiang, Z. L. Yin, Y. H. Zhang, X. H. Li, *Electrochim. Acta* 2013, 91, 214.
- [14] a) Z. W. Jing, S. N. Wang, Q. Fu, V. Baran, A. Tayal, N. P. M. Casati, A. Missyul, L. Simonelli, M. Knapp, F. J. Li, H. Ehrenberg, S. Indris, C. X. Shan, W. B. Hua, *Energy Storage Mater.* 2023, 59; b) C. Cui, X. Fan, X. Zhou, J. Chen, Q. Wang, L. Ma, C. Yang, E. Hu, X.-Q. Yang, C. Wang, *J. Am. Chem. Soc.* 2020, 142, 8918.
- [15] a) J. Y. Baek, H. W. Ha, I. Y. Kim, S. J. Hwang, *J. Phys. Chem. C* 2009, 113, 17392; b) G. Z. Wei, X. Lu, F. S. Ke, L. Huang, J. T. Li, Z. X. Wang, Z. Y. Zhou, S. G. Sun, *Adv. Mater.* 2010, 22, 4364; c) L. Chen, Y. Su, S. Chen, N. Li, L. Bao, W. Li, Z. Wang, M. Wang, F. Wu, *Adv. Mater.* 2014, 26, 6756; d) M. Xu, L. Fei, W. Zhang, T. Li, W. Lu, N. Zhang, Y. Lai, Z. Zhang, J. Fang, K. Zhang, J. Li, H. Huang, *Nano Lett.* 2017, 17, 1670; e) H. M. Zhou, Z. H. Yang, C. J. Yin, S. L. Yang, J. Li, *Ceram. Int.* 2018, 44, 20514; f) F. Fu, Y. Yao, H. Wang, G.-L. Xu, K. Amine, S.-G. Sun, M. Shao, *Nano Energy* 2017, 35, 370.
- [16] a) J. Yang, X. Zhang, X. Han, F. Cheng, Z. Tao, J. Chen, *J. Mater. Chem. A* 2013, 1, 13742; b) J. Yang, F. Cheng, X. Zhang, H. Gao, Z. Tao, J. Chen, *J. Mater. Chem. A* 2014, 2, 1636.
- [17] C. Q. Shen, K. Zhou, W. Lin, P. Yang, X. Y. Hu, L. B. Wang, *Appl. Surf. Sci.* 2024, 657.
- [18] a) S. Zhao, Z. Guo, K. Yan, S. Wan, F. He, B. Sun, G. Wang, *Energy Storage Mater.* 2021, 34, 716; b) H. Chen, C. Sun, *Chem. Commun.* 2023, 59, 9029.
- [19] a) A. Baniya, M. B. Saud, H. Li, M. B. Faheem, Y. Zhang, A. Thapa, R. S. Bobba, P. I. Kaswekar, Q. Qiao, *Sustain. Energ. Fuels* 2024, 8, 3574; b) W. Tu, L. Xing, P. Xia, M. Xu, Y. Liao, W. Li, *Electrochim. Acta* 2016, 204, 192; c) Y. Ma, Y. Zhou, C. Du, P. Zuo, X. Cheng, L. Han, D. Nordlund, Y. Gao, G. Yin, H. L. Xin, M. M. Doeff, F. Lin, G. Chen, *Chem. Mater.* 2017, 29, 2141; d) S. Gu, Y. Cui, K. Wen, S. Chen, J. Zhao, *J. Alloys Comp.* 2020, 829; e) P. Z. Kou, Z. G. Zhang, Z. Y. Wang, R. G. Zheng, Y. G. Liu, F. Lv, N. Xu, *Energy Fuels* 2023, 37, 18243; f) J. Dong, F. Wu, J. Zhao, Q. Shi, Y. Lu, N. Li, D. Cao, W. Li, J. Hao, X. Yang, L. Chen, Y. Su, *Energy Storage Mater.* 2023, 60; g) Z. Feng, L. Guo, X. Liu, W. Li, R. Zhang, D. Wang, W. Zhang, W. Zheng, *ACS Appl. Energy Mater.* 2024, 7, 2791.
- [20] a) J. Zhou, X. Lian, Q. Shi, Y. Liu, X. Yang, A. Bachmatiuk, L. Liu, J. Sun, R. Yang, J.-H. Choi, M. H. Rummeli, *Adv. Energy Sustain. Res.* 2022, 3; b) K. Gao, F. Yin, F. Mi, C. Sun, *ACS Appl. Mater. Interfaces* 2025, 17, 32511.
- [21] J. Chen, A. Gutierrez, M. A. Sultanov, J. Wen, J. R. Croy, Y. Wang, V. Srinivasan, P. Barai, *ACS Appl. Energy Mater.* 2024, 7, 2167.
- [22] a) J. Li, R. Yan, B. Xiao, D. T. Liang, D. H. Lee, *Energy Fuels* 2008, 22, 16; b) S. Lu, C. Yang, M. Nie, *J. Alloys Comp.* 2017, 708, 780.
- [23] a) M. A. Garakani, S. Abouali, B. Zhang, C. A. Takagi, Z. L. Xu, J. Q. Huang, J. Q. Huang, J. K. Kim, *Acs Appl. Mater. Interfaces* 2014, 6, 18971; b) H. B. Li, X. C. Duan, J. M. Ma, W. J. Zheng, *Cryst. Res. Technol.* 2012, 47, 25; c) J. Zhao, R. Pathak, Z. Zhao, X. Chen, M. B. Saud, H. Li, F. Wu, Q. Qiao, J. W. Elam, X. Wang, *Green Chem.* 2023, 25, 10182.
- [24] F. Liu, J. Li, C. Chen, D. Ning, J. Yang, Z. Chu, X. Mao, Y. Lan, *Res. Chem. Intermed.* 2022, 48, 3007.
- [25] J. Sicklinger, M. Metzger, H. Beyer, D. Pritzl, H. A. Gasteiger, *J. Electrochem. Soc.* 2019, 166, A2322.
- [26] J. Zheng, Y. Ye, T. Liu, Y. Xiao, C. Wang, F. Wang, F. Pan, *Acc. Chem. Res.* 2019, 52.
- [27] a) S. Shi, T. Wang, M. Cao, J. Wang, M. Zhao, G. Yang, *Acs Appl. Mater. Interfaces* 2016, 8, 11476; b) R. Yu, X. Zhang, T. Liu, X. Xu, Y. Huang, G. Wang, X. Wang, H. Shu, X. Yang, *ACS Sustain. Chem. Eng.* 2017, 5, 8970.
- [28] R. E. Ruther, A. F. Callender, H. Zhou, S. K. Martha, J. Nanda, *J. Electrochem. Soc.* 2014, 162, A98.
- [29] a) D. Tewari, A. Gutierrez, J. Croy, V. Srinivasan, *Chem. Mater.* 2024, 36, 10922; b) Z. Fang, W. Li, B. Zhao, J. Bai, K. Li, H. Ma, X. Zhu, Y. Sun, *ACS Appl. Energy Mater.* 2021, 4, 10986.
- [30] B. L. Bales, L. Messina, A. Vidal, M. Peric, O. R. Nascimento, *J. Phys. Chem. B* 1998, 102, 10347.
- [31] G. Duplatre, M. F. Ferreira Marques, M. da Graça Miguel, *J. Phys. Chem.* 1996, 100, 16608.
- [32] W. He, P. Liu, Y. Zhou, H. Zheng, Z. Zheng, B. Liu, J. Yuan, Q. Zhang, L. Wang, Q. Luo, Q. Xie, B. Qu, D.-L. Peng, *Sustain. Mater. Technol.* 2020, 25, e00171.
- [33] a) M. Xu, L. Fei, W. Zhang, T. Li, W. Lu, N. Zhang, Y. Lai, Z. Zhang, J. Fang, K. Zhang, J. Li, H. Huang, *Nano Lett.* 2017, 17, 1670; b) Y. Xie, F. Wu, X. Dai, Y. Mai, Y. Gu, H. Jin, J. Li, *Int. J. Energy Res.* 2020, 45, 6041.
- [34] Y.-C. Chien, H. Liu, A. S. Menon, W. R. Brant, D. Brandell, M. J. Lacey, *Nat. Commun.* 2023, 14, 2289.
- [35] C. Yin, Z. N. Wei, M. H. Zhang, B. Qiu, Y. H. Zhou, Y. G. Xiao, D. Zhou, L. Yun, C. Li, Q. W. Gu, W. Wen, X. Li, X. H. Wen, Z. P. Shi, L. H. He, Y. S. Meng, Z. P. Liu, *Mater. Today* 2021, 51, 15.

Manuscript received: May 28, 2025

Revised manuscript received: June 24, 2025

Version of record online: